Acta Oceanol. Sin., 2024, Vol. 43, No. 7, P. 78–92
https://doi.org/10.1007/s13131-023-2184-8
http://www.aosocean.com
E-mail: ocean2@hyxb.org.cn

Potential morphological responses of an artificial beach to a flood in extreme events: field observation and numerical modelling

Jiadong Fan[1], Cuiping Kuang[1]*, Xuejian Han[1], Lixin Gong[2, 3]*, Huixin Liu[2, 3], Jiabo Zhang[2, 3]

[1] College of Civil Engineering, Tongji University, Shanghai 200082, China

[2] The Eighth Geological Brigade, Hebei Geological and Mineral Exploration Development Bureau, Qinhuangdao 066001, China

[3] Marine Ecological Restoration and Smart Ocean Engineering Research Center of Hebei Province, Qinhuangdao 066001, China

Received 26 October 2023; accepted 18 January 2024

Abstract

Conch Island is a typical artificial island at the Tanghe Estuary in Bohai Sea, China. To improve natural environment and boost local tourism, beach nourishment will be applied to its north-western shore. The projected beach is landward and opposite to the Jinmeng Bay Beach. Nowadays, with climate changes, frequent heavy rainfalls in Hebei Province rise flood hazards at the Tanghe Estuary. Under this circumstance, potential influences on the projected beach of a flood are investigated for sustainable managements. A multi-coupled model is established and based on the data from field observations, where wave model, flow model and multi-fraction sediment transport model are included. In addition, the impacts on the projected beach of different components in extreme events are discussed, including the spring tides, storm winds, storm waves, and sediment inputs. The numerical results indicate the following result. (1) Artificial islands protect the coasts from erosion by obstructing landward waves, but rise the deposition risks along the target shore. (2) Flood brings massive sediment inputs and leads to scours at the estuary, but the currents with high sediment concentration contribute to the accretions along the target shore. (3) The projected beach mitigates flood actions and reduces the maximum mean sediment concentration along the target shore by 20%. (4) The storm winds restrict the flood and decrease the maximum mean sediment concentration by 21%. With the combined actions of storm winds and waves, the maximum value further declines by 38%. (5) A quadratic polynomial relationship between the deposition depths and the maximum sediment inputs with flood is established for estimations on the potential morphological changes after the flood process in extreme events. For the uncertainty of estuarine floods, continuous monitoring on local hydrodynamic variations and sediment characteristics at Tanghe Estuary is necessary.

Key words: beach nourishment, flood, artificial island, sediment transport, extreme events, storm

Citation: Fan Jiadong, Kuang Cuiping, Han Xuejian, Gong Lixin, Liu Huixin, Zhang Jiabo. 2024. Potential morphological responses of an artificial beach to a flood in extreme events: field observation and numerical modelling. Acta Oceanologica Sinica, 43(7): 78–92, doi: 10.1007/s13131-023-2184-8

1 Introduction

Nowadays, non-structural measures have been widely applied to coastal restorations (Zhong et al., 2021). In particular, beach nourishment has been proved to be an effective approach to mitigate excessive erosions and recessions along coasts of the Bohai Sea, involving Tiger-Rock Beach (Kuang et al., 2019), Jinmeng Bay Beach (Xie et al., 2013) and Beidaihe Beach (Zhang et al., 2012; Kuang et al., 2011). Moreover, nourished beaches can provide public leisure spaces to stimulate the development of coastal tourism. To attract tourists and achieve economic benefits further, artificial islands projects are popular in recent decades. However, continuous development activities not only affect functions of soft structures, but also alter local hydrodynamic conditions considerably. Researches on Chinese coasts provide massive experiences for construction and management issues of artificial islands. For instance, with the construction of Nanhaimingzhu artificial island, local dynamic conditions changes in the Haikou Bay. In details, it is found that the artificial island hinders currents and waves, and results in massive depositions in its cover areas (Xiao, 2021; Xiao et al., 2022). Meanwhile, the currents are intensified on both sides of the artificial island, which causes great erosions on the coast, so He et al. (2021) and Li (2018) suggested that beach nourishment should be utilized for essential protections, and such approach is also applicable to the Hongtang Bay in Sanya, Hainan (Li, 2021) and the Riyue Bay in Wanning, Hainan (Shi et al., 2015). According to field observations (Zhang et al., 2022; Li et al., 2019), the interactions between two artificial islands bring about much more erosions on the coast for intensive diffraction in the Riyue Bay. Apart from coasts, shores of artificial islands are also faced with the risks of erosions.

Foundation item: The National Key Research and Development Program of China under contract No. 2022YFC3106205; the National Natural Science Foundation of China under contract Nos 41976159 and 41776098.

*Corresponding author, E-mail: cpkuang@tongji.edu.cn; gonglixin83@163.com

For example, the flow velocities along Ruyi Island in Qiongzhou Strait vary by about 45%, which may cause excessive erosions (Wang et al., 2013a). Thus, researches on sediment transport around artificial islands are popular in the recent decade in particular.

Han et al. (2007, 2009) constructed a series of physical models to simulate scours around coastal structures on a silt-sandy bed, and they coupled storm waves with spring tides for simulations. The results indicated that both storm waves and spring tides intensify the scours around an artificial island in terms of the erosion thickness and width, where rock armours are of great stability for protection under extreme events. Such phenomena are more evident for an artificial island which is close to the coast, where the littoral currents are accelerated due to reduced cross-sections between the island and the coast (Lin, 2017), and the littoral sediment transport is intensive simultaneously (Song, 2014). In addition, Zhong (2017) and Zou (2020) concentrated on the influences on an artificial island by a typhoon, and they found that artificial islands can hinder the typhoons and protect the coast from erosion, but for the exposed coast, beach nourishment is an effective approach for defence, as well as armour blocks (Li, 2015). Apart from marine conditions, river conditions are also significant to an artificial island at estuary (Liu et al., 2021; Ban and Wu, 2018). Sheng et al. (2016) and Zhang (2013) investigated the influences on Conch Island of a flood from the Tanghe Estuary, where the flood brings about massive sediment input and alter local morphological conditions in a short term. The construction of Conch Island affects the flow directions of flood and changes local sediment transport. Therefore, the extensions of Conch Island may alter local hydrodynamic conditions and lead a new trend of morphological evolution further.

As an international resort in the Bohai Sea of China, Conch Island is named after its layout and famous for the entertainment, aquatic sports and Yacht industry. With such comprehensive benefits, it plays a significant role in the development of local economy. However, poor management resulted in environment deterioration and biodiversity loss along the north-western shore of Conch Island. Therefore, the north-western shore is projected to be rebuilt by beach nourishment to improve its environment and attraction for a sustainable development. To investigate potential morphological responses of the projected beach along Conch Island, it is essential to focus on the floods from the Tanghe Estuary. A multi-coupled model is established and based on the data from recent surveys. The simulations are realized by MIKE 21 Flow Model (FM), where wave model, flow model, and sediment transport model are coupled together. Extreme events are designed under a storm in July 2021 for the investigation. Furthermore, influences of different components in extreme events are discussed. The present study aims to provide a feasible approach to estimate the morphological changes of the projected beach after a flood for effective management.

2 Materials and methods

2.1 *Research area*

Conch Island is located at the Tanghe Estuary of Qinhuangdao, along the west coasts of the Bohai Sea (Fig. 1). The research area (Fig. 2) covers the Tanghe Estuary, Conch Island, Jinmeng Bay Beach, and Lotus Island mainly. The Tanghe River is 28.5 km in length and consists of two branches. The east branch (EB) is larger than the west branch (WB). A numerical model of Qinhuangdao nearshore area is established by MIKE 21 FM under Beijing Geodetic Coordinate System 1954 (Fig. 3). The modelling area extends from Ledao Ocean Park in north to the Yanghe Estuary in south, with the length of 35.6 km along shore (NE–SW) and 16.5 km off shore (NW–SE). The total water area is approximately 587.4 km^2, containing 22 942 nodes and 44 148 meshes. The grid length ranges from 4 m to 3 200 m (Fig. 3). The boundary conditions of open sea are provided by the Bohai Sea model, which has been introduced and validated in the previous research (Han et al., 2022).

The bathymetric data are based on a field survey in 2016 by Tianjin Exploration Centre of Marine Geology. The details about the survey can be referred to the previous research (Kuang et al., 2022). The bathymetry of Jinmeng Bay Beach is updated partially by the beach-profile survey with RTK (real-time kinematic) technique by the Eighth Geological Brigade of Hebei Geological Prospecting Bureau in August 2021 (Fig. 4).

Jinmeng Bay Beach was rebuilt by beach nourishment for berms and sandbars in 2010s, and the nourished beach profile can be treated as a smooth surface after the restoration (Xie et al., 2013). Figure 5 shows the observed data from a survey in August 2021, and the profiles are divided into three groups by their positions for analysis, where P1–P3 are close to Lotus Island; P4–P6 are between the two artificial islands; P7–P9 are close to Conch Island. As is shown in Fig. 5, the nearshore bed level of beaches covered by artificial islands (P1–P3 and P7–P9) are higher than those of open coasts (P4–P6), which means that artificial islands

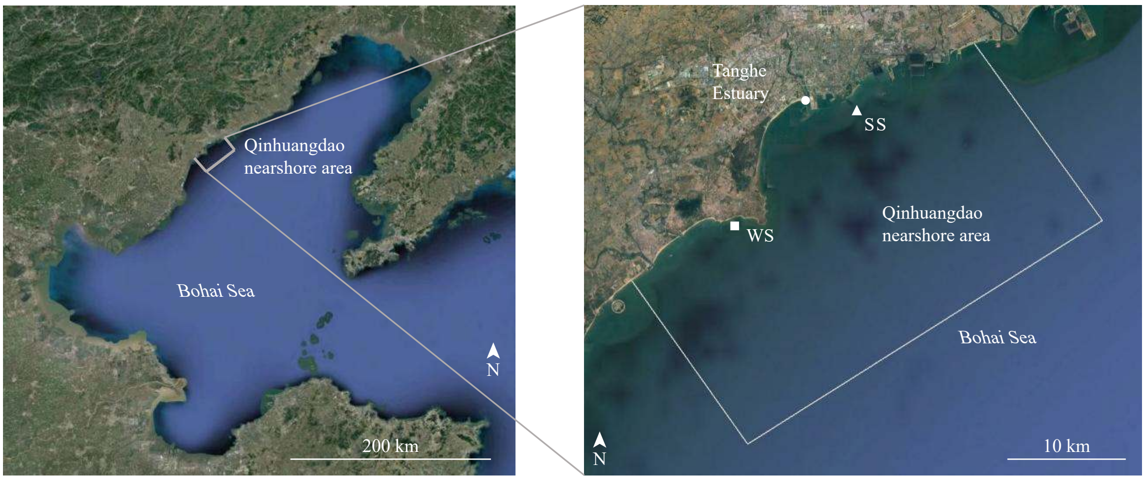

Fig. 1. Qinhuangdao nearshore area for simulation.

Fig. 2. Site of the research area.

hinder landward actions from the open sea and defend the shore from erosion effectively. In addition, for open coasts, depositions occur on seaward sides of submerged sandbars and erosions occur on berms mainly (P4 and P5), where the sediment transport has a seaward trend. In cover areas of Lotus Island (P1 and P2), the generations of berms indicate that depositions dominate local morphological evolution. Particularly, the berms covered by Conch Island (P7–P9) are more evident due to its impermeable structure. Moreover, depositions occur within the distance from 400 m to 600 m, which results from the littoral sediment transport mainly. In a brief summary, in cover areas generated by Conch Island, where the projected beach is, deposition might be a main risk for the shore, because the littoral sediment transport dominates the morphological evolutions.

According to the project design by Qinghuangdao Qinzheng Real Estate Development Co., Ltd. (2021), the projected beach on the north-western shore of Conch Island extends 350 m in length. The intersecting profile (Dean, 1991) is utilized with a slope as 1:10. The designed berm under beach nourishment is 15 m in width with the top elevation as 2 m (1985 National Elevation Datum of China). The total volume of nourishment is 11.5×10^4 m^3. Figure 6 shows bathymetries of the research area by the bare shore and the projected beach, respectively.

2.2 *Methods*

Hydrodynamic module and spectral wave module of MIKE 21 FM are coupled for simulations to include wave actions in real-world conditions. In addition, mud transport module is utilized to simulate the morphological impacts on the projected beach of a flood. Following governing equations can be referred to the manual of MIKE 21 FM, which is accessible on the official website of MIKE (https://www.mikepoweredbydhi.com/, accessed on August 15, 2023).

2.2.1 *Hydrodynamic module*

In this investigation, there is no source involved, so relative items are removed from the initial equations. The governing equations of hydrodynamic module are anchored in the integrations of continuity equation [Eq. (1)] and horizontal momentum equations [Eqs (2) and (3)] over depth as follows.

$$\frac{\partial h}{\partial t}+\frac{\partial h\bar{u}}{\partial x}+\frac{\partial h\bar{v}}{\partial y}=0, \tag{1}$$

$$\frac{\partial h\bar{u}}{\partial t}+\frac{\partial h\bar{u}^2}{\partial x}+\frac{\partial h\bar{u}\,\bar{v}}{\partial y}=f\bar{v}h-gh\frac{\partial \eta}{\partial x}-\frac{h}{\rho_0}\frac{\partial p_{\rm a}}{\partial x}+\frac{\tau_{\rm sx}}{\rho_0}-\frac{\tau_{\rm bx}}{\rho_0}-\frac{1}{\rho_0}\left(\frac{\partial s_{xx}}{\partial x}+\frac{\partial s_{xy}}{\partial y}\right)+\frac{\partial}{\partial x}\left(hT_{xx}\right)+\frac{\partial}{\partial y}\left(hT_{xy}\right), \tag{2}$$

$$\frac{\partial h\bar{v}}{\partial t}+\frac{\partial h\bar{u}\,\bar{v}}{\partial x}+\frac{\partial h\bar{v}^2}{\partial y}=-f\bar{u}h-gh\frac{\partial \eta}{\partial y}-\frac{h}{\rho_0}\frac{\partial p_{\rm a}}{\partial y}+\frac{\tau_{\rm sy}}{\rho_0}-\frac{\tau_{\rm by}}{\rho_0}-\frac{1}{\rho_0}\left(\frac{\partial s_{yx}}{\partial x}+\frac{\partial s_{yy}}{\partial y}\right)+\frac{\partial}{\partial x}\left(hT_{xy}\right)+\frac{\partial}{\partial y}\left(hT_{yy}\right), \tag{3}$$

where $h=\eta+d$ is the total water depth; η is the surface elevation and d is the still water depth; t is the time; $\bar{u}$ and $\bar{v}$ are the depth-averaged velocities; $f=2\Omega\sin\phi$ is the Coriolis parameter; Ω is the angular rate of revolution and ϕ is the geographic latitude; g is the gravitational acceleration; ρ_0 is the density of water; $p_{\rm a}$ is the atmospheric pressure; $(\tau_{\rm sx}, \tau_{\rm sy})$ and $(\tau_{\rm bx}, \tau_{\rm by})$ are the x and y components of the surface wind and bottom stresses; s_{xx}, s_{xy}, s_{yx}, and s_{yy} are components of the radiation stress tensor; T_{xx}, T_{xy}, and T_{yy} are the lateral stresses, including viscous friction, turbulent friction and differential advection. The surface stress $\vec{\tau_{\rm s}}=(\tau_{\rm sx}, \tau_{\rm sy})$ is determined by the wind above the surface based on an empirical relation as follows:

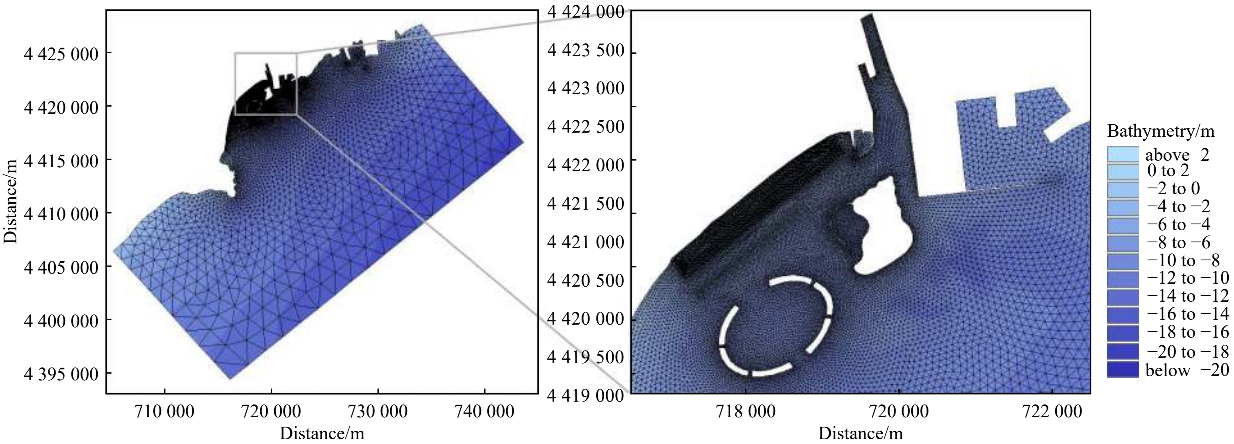

Fig. 3. Meshes of the research area.

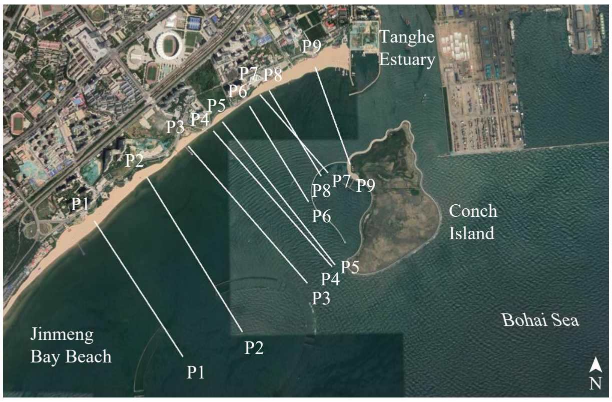

Fig. 4. Sections of beach-profile survey on Jinmeng Bay Beach in August 2021.

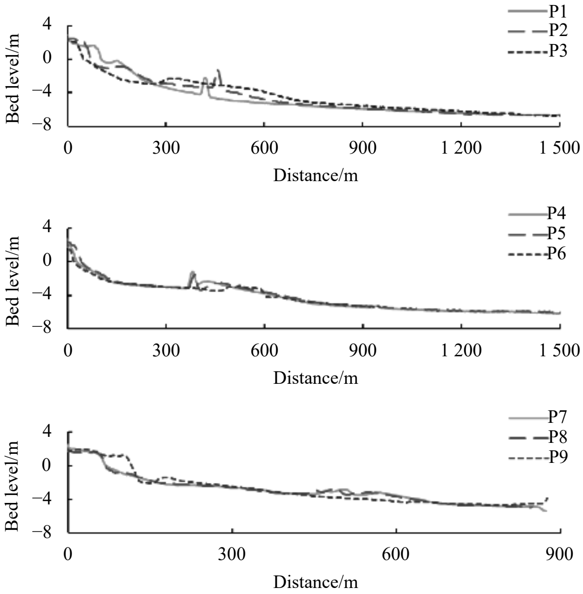

Fig. 5. Beach profiles of Jinmeng Bay Beach measured in August 2021.

$$\vec{\tau_s} = \rho_a c_d \left|\vec{u_w}\right| \vec{u_w}, \tag{4}$$

where $\vec{u_w} = (u_w, v_w)$ is the wind speed 10 m above the sea surface; ρ_a is the density of air. The hourly data of $\vec{u_w}$ are available on the European Centre for Medium-Range Weather Forecasts (ECMWF) [ERA5 hourly data on single levels from 1959 to present (copernicus.eu), accessed on August 15, 2023]. The drag coefficient c_d in Eq. (4) can be calculated by the following empirical formula proposed by Wu (1980, 1994).

$$c_d = \begin{cases} c_a, & w_{10} < w_a, \\ c_a + \dfrac{c_b - c_a}{w_b - w_a}\left(w_{10} - w_a\right), & w_a \leqslant w_{10} < w_b, \\ c_b, & w_{10} \geqslant w_b, \end{cases} \tag{5}$$

where w_{10} is the wind velocity 10 m above the sea surface; c_a, c_b, w_a, and w_b are the empirical factors with the default values as $c_a = 1.255 \times 10^{-3}$, $c_b = 2.425 \times 10^{-3}$, $w_a = 7$ m/s and $w_b = 25$ m/s. The bottom stress $\vec{\tau_b} = (\tau_{bx}, \tau_{by})$ in Eqs (2) and (3) is determined by a quadratic friction law as follows:

$$\vec{\tau_b} = \rho_0 c_f \vec{u_b} \left|\vec{u_b}\right|, \tag{6}$$

where $\vec{u_b} = (u, v)$ is the flow velocity above the bottom, which equals to the depth-average velocity for two-dimensional calculations; c_f is the drag coefficient determined by the Manning number in this simulation.

$$c_f = \frac{g}{\left(Mh^{1/6}\right)^2}, \tag{7}$$

where the Manning number M is generally given by 74 $m^{1/3}$/s in the Bohai Sea (Kuang et al., 2022). Moreover, the radiation stress tensor in Eqs (2) and (3) dominates the coupling between hydrodynamic module and spectral wave module in MIKE 21 FM, and the components can be calculated as

$$\begin{cases} s_{xx} = E\left[(2n - 1/2) - n\sin^2\theta\right], \\ s_{xy} = s_{yx} = E\,n\cos^2\theta, \\ s_{yy} = E\left[(n - 1/2) + n\sin^2\theta\right], \end{cases} \tag{8}$$

where $E = \rho g H^2/8$ is the wave energy and H is the wave height; $n = c_g/c$ is the transfer rate; c_g is the magnitude of the group velocity [Eq. (9)] and c is the phase velocity [Eq. (10)]; θ is the wave direction.

$$c_g = \frac{\partial\sigma}{\partial k} = \frac{1}{2}\left[1 + \frac{2kh}{\sinh(2kh)}\right]\frac{\sigma}{k}, \tag{9}$$

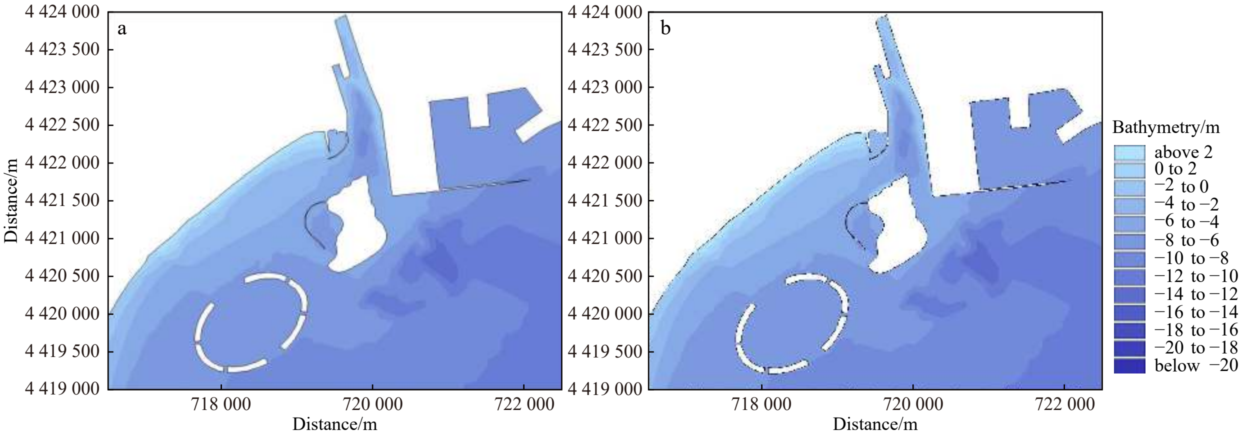

Fig. 6. Bathymetries of the research area by the bare shore (a) and the projected beach (b).

$$c = \frac{\sigma}{k}, \tag{10}$$

where k is the magnitude of the wave number vector $\vec{k}$; σ is the relative angular frequency. In addition, the lateral stresses in Eqs (2) and (3) can be estimated by an eddy viscosity formulation based on $\bar{u}$ and $\bar{v}$ as follows.

$$T_{xx} = 2A\frac{\partial \bar{u}}{\partial x}, \tag{11}$$

$$T_{xy} = A\left(\frac{\partial \bar{u}}{\partial y} + \frac{\partial \bar{v}}{\partial x}\right), \tag{12}$$

$$T_{yy} = 2A\frac{\partial \bar{v}}{\partial y}, \tag{13}$$

where A is the horizontal eddy viscosity, and the sub-grid scale eddy viscosity can be calculated by Eq. (14) given by Smagorinsky (1963).

$$A = c_s^2 l^2 \sqrt{2S_{ij}S_{ij}}, \tag{14}$$

where c_s is a constant, which is set as 0.28 in this study; l is the characteristic length and the deformation rate S_{ij} is given by

$$S_{ij} = \frac{1}{2}\left(\frac{\partial u_i}{\partial x_j} + \frac{\partial u_j}{\partial x_i}\right),\ i, j = 1, 2. \tag{15}$$

2.2.2 *Spectral wave model*

Spectral wave module is described by the transport equation for wave action density.

$$N = \frac{E}{\sigma}, \tag{16}$$

where $N(\sigma, \theta)$ is the wave action density; $E(\sigma, \theta)$ is the energy density. In horizontal Cartesian co-ordinates, the conservation equation for wave action can be written as

$$\frac{\partial N}{\partial t} + \nabla\cdot\left(\vec{v}N\right) = \frac{S}{\sigma}, \tag{17}$$

where $N(\vec{x}, \sigma, \theta, t)$ is the action density; $\vec{x} = (x, y)$ is the Cartesian co-ordinates; ∇ is the four-dimensional differential operator; $\vec{v} = (c_x, c_y, c_\sigma, c_\theta)$ is the propagation velocity of a wave group in the four-dimensional phase space; S is the source term for the energy balance equation. The four characteristic propagation speeds as follows:

$$\left(c_x, c_y\right) = \frac{\mathrm{d}\vec{x}}{\mathrm{d}t} = \vec{c_g} + \vec{U}, \tag{18}$$

$$c_\sigma = \frac{\mathrm{d}\sigma}{\mathrm{d}t} = \frac{\partial\sigma}{\partial h}\left[\frac{\partial h}{\partial t} + \vec{U}\cdot\nabla_{\vec{x}}h\right] - c_g\vec{k}\cdot\frac{\partial\vec{U}}{\partial s}, \tag{19}$$

$$c_\theta = \frac{\mathrm{d}\theta}{\mathrm{d}t} = -\frac{1}{k}\left[\frac{\partial\sigma}{\partial h}\frac{\partial h}{\partial m} + \vec{k}\cdot\frac{\partial\vec{U}}{\partial m}\right], \tag{20}$$

where $\vec{U} = (u, v)$ is the flow velocity; $\nabla_{\vec{x}}$ is the two-dimensional differential operator in the $\vec{x}$-space; s is the space co-ordinate in the wave direction θ; m is a co-ordinate perpendicular to s. Furthermore, the energy source term S represents the superposition of source functions as

$$S = S_{\mathrm{in}} + S_{\mathrm{nl}} + S_{\mathrm{ds}} + S_{\mathrm{bot}} + S_{\mathrm{surf}}, \tag{21}$$

where S_{in} is the generation of energy by wind; S_{nl} is the wave energy transfer due to non-linear wave-wave interaction; S_{ds} is the dissipation of wave energy due to white capping; S_{bot} is the dissipation due to bottom friction; S_{surf} is the dissipation of wave energy due to depth-induced breaking.

2.2.3 *Mud transport module*

Mud transport module is based on the advection-dispersion equation.

$$\frac{\partial h\bar{c}}{\partial t} + \frac{\partial hu\bar{c}}{\partial x} + \frac{\partial hv\bar{c}}{\partial y} = \frac{\partial}{\partial x}\left(D_x\frac{\partial h\bar{c}}{\partial x}\right) + \frac{\partial}{\partial y}\left(D_y\frac{\partial h\bar{c}}{\partial y}\right) - hS_{\mathrm{ND}}, \tag{22}$$

where $\bar{c}$ is depth averaged concentration; D_x and D_y are the dispersion coefficients; $S_{\mathrm{ND}} = S_{\mathrm{D}} - S_{\mathrm{E}}$ is the net deposition term; S_{D} and S_{E} are the deposition item and erosion item. For cohesive sediments, the deposition item can be calculated as Eq. (23) given by Krone (1962),

$$S_{\mathrm{D}} = w_{\mathrm{s}}c_{\mathrm{b}}p_{\mathrm{d}}, \tag{23}$$

where w_{s} is the settling velocity; c_{b} is the near bed concentration; p_{d} is the probability of deposition,

$$p_{\mathrm{d}} = 1 - \frac{\tau_{\mathrm{b}}}{\tau_{\mathrm{cd}}}\tau_{\mathrm{b}} \leqslant \tau_{\mathrm{cd}}, \tag{24}$$

where τ_{b} is the bed shear stress; τ_{cd} is the critical bed shear stress for deposition. The near bed concentration is related to the depth averaged concentration (Teeter, 1986),

$$\beta = \frac{c_{\mathrm{b}}}{\bar{c}}, \tag{25}$$

$$\beta = 1 + \frac{P_{\mathrm{e}}}{1.25 + 4.75{p_{\mathrm{d}}}^{2.5}}, \tag{26}$$

$$P_{\mathrm{e}} = \frac{6w_{\mathrm{s}}}{\kappa U_{\mathrm{f}}}, \tag{27}$$

where P_{e} is the Peclet number; κ is Von Karman's universal constant, $\kappa = 0.4$; $U_{\mathrm{f}} = \sqrt{\tau_{\mathrm{b}}/\rho}$ is the friction velocity. Meanwhile, for dense, consolidated bed the erosion is defined as

$$S_{\mathrm{E}} = G\left(\frac{\tau_{\mathrm{b}}}{\tau_{\mathrm{ce}}} - 1\right)^n,\ \tau_{\mathrm{b}} > \tau_{\mathrm{ce}}, \tag{28}$$

where G is the erodibility of bed; τ_{ce} is the critical bed shear stress for erosion; n is the power of erosion.

In MIKE 21 FM Mud transport module, fine sand fraction can be activated for simulation. The erosion item and the deposition item are given by

$$S_e = \left(\frac{\bar{c}_e - \bar{c}}{t_s}\right),\ \bar{c}_e > \bar{c}, \tag{29}$$

$$S_d = -\left(\frac{\bar{c}_e - \bar{c}}{t_s}\right),\ \bar{c}_e < \bar{c}, \tag{30}$$

where $\bar{c}_e$ is depth-averaged equilibrium concentration; $\bar{c}$ is a compound concentration; t_s is a time-scale

$$t_s = \frac{h_s}{w_s}, \tag{31}$$

where h_s is the average water depth.

$$\bar{c}_e = \frac{q_s}{\bar{u}h}, \tag{32}$$

$$q_s = \int_a^h c_s u \cdot \mathrm{d}z, \tag{33}$$

where q_s is the suspended load transport; $\bar{u}$ is the depth averaged flow velocity; c_s and u are the sediment concentration and flow velocity at distance z from bed, respectively; a is the layer thickness, which equals to the equivalent roughness height.

2.3 *Model setup*

2.3.1 *Sediment characteristics*

According to previous researches (Sheng et al., 2016; Xie et al., 2013) and recent surveys on Jinmeng Bay Beach by utilization of laser particle size analysers in 2021. There are two main kinds of sediments in the research area, including silts and sands. The grain-sizes of silts range from 0.05 mm to 0.07 mm, while the grain-sizes of sands range between 0.15 mm and 0.23 mm. Thus, two sediment fractions are set for the present investigation with uniform grain-sizes, silt fraction ($d_{50} = 0.06$ mm) and sand fraction ($d_{50} = 0.20$ mm), respectively.

The grain-size of silts is larger than 0.03 mm, so the flocculation of silts can be neglected (Wang et al., 2013b). Sediment settling velocity w_s can be calculated by Stokes's formula [Eq. (34)] (Cheng, 1997).

$$w_s = \frac{1.65 g {d_{50}}^2}{18\upsilon}, \tag{34}$$

where g is gravitational acceleration, 9.81 m/s^2; υ is water viscosity, 1.01×10^{-6} m^2/s; d_{50} is 50 percent fractile of grain-size of sediment. Settling velocity of sands ($d_{50} = 0.20$ mm) is calculated as 0.036 m/s and that of flocculated silts ($d_{50} = 0.06$ mm) is 0.003 2 m/s. According to the empirical relation (Cao and Wang, 1994), the critical deposition shear stress τ_{cd} equals 4/9 of the critical erosion shear stress τ_{ce}, and the critical erosion shear stress can be calculated by Eq. (35) given by Tang (1963).

$$\tau_{ce} = \frac{1}{77.5}\left[3.2\left(\rho_s - \rho\right) g d_{50} + \left(\frac{\sigma}{\sigma_0}\right)^{10} \frac{C}{d_{50}}\right], \tag{35}$$

where $\rho_s = 2.65 \times 10^3$ kg/m^3 is the density of sediment grains; ρ is the density of water; σ/σ_0 represents stability of volumetric weight, and it equals 1 for consolidated mud; $C = 2.9 \times 10^{-5}$ kg/m is a constant. Thus, the critical erosion shear stress of the silt ($d_{50} = 0.06$ mm) is estimated by 0.065 N/m^2, and its critical deposition shear stress is set as 0.029 N/m^2. The critical erosion shear stress of the sand ($d_{50} = 0.20$ mm) is estimated by 0.032 N/m^2, and its critical deposition shear stress is set as 0.014 N/m^2.

2.3.2 *Bed layer characteristics*

According to the detailed sedimentologic information by Wang (2014), two types of layers are set for the sea bed. The additional layers represent artificial sand beaches, covering Jinmeng Bay Beach and the projected beach, respectively, and the bed layer is 2 m in thickness. Table 1 shows the details of the layers.

In addition, the equivalent roughness height k_s is estimated by

$$k_s = 2d_{50}, \tag{36}$$

where k_s is set as 0.000 12 m by grain-size of silts ($d_{50} = 0.06$ mm).

2.3.3 *Flood process*

Sheng et al. (2016) introduced an approach to design the flood hydrograph of the Tanghe River. Same magnification method is utilized to design the flood, which is based on the recorded flood No. 980713 at Qinhuangdao Station. The maximum sediment input with the flood is referred to the records in Shihe Reservoir on July 29, 1991 as 0.16 kg/m^3. This value matched the average annual sediment concentration at the Tanghe Estuary (Sheng et al., 2016).

Table 2 and Fig. 7 show the details of the designed flood process.

2.3.4 *Scenarios*

To investigate potential responses of the projected beach to a flood in extreme events, four scenarios are simulated under real-world conditions in July 2021 during a storm. Figure 8 shows peak wind vector field during the storm. Table 3 contains more information about the scenarios.

2.4 *Validation*

The wave model is validated by the observation at WS (Fig. 1)

Table 1. Sediment characteristics of each layer

Layer	Sediment fraction	Description	Layer thickness/m	Dry density/(kg·m^{-3})
Additional layers	sand	artificial sand beaches	varying	1 304
Bed layer	silt	hard mud	2	1 046

Table 2. Designed flood of the Tanghe River

River branch	Return period	Covering area/m^2	Maximum discharge/(m^3·s^{-1})	Maximum sediment input/(kg·m^{-3})
EB	50-year	184.0	1 618	0.16
WB	50-year	53.7	598	0.06

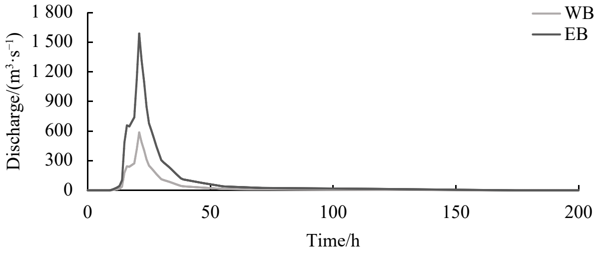

a. designed flood hydrographs

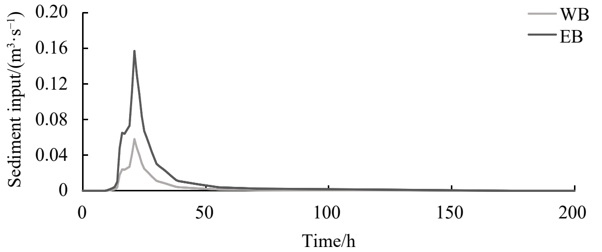

b. designed sediment inputs

Fig. 7. Designed flood process in EB and WB of the Tanghe Estuary, including designed flood hydrographs (a) and designed sediment inputs (b).

in June 2020. Figure 9 shows validations of significant wave height, mean wave period, and mean wave direction. The trends of simulated values match well with the observed data.

Both sediment concentration and beach profiles are validated for sediment transport model. The sediment concentration was collected at SS (Fig. 1) during October 18 to 19, 2016. The beach profiles for validation (Fig. 4) were measured in April 2022. Figures 10 and 11 show validations of sediment concentration and beach profiles, respectively. The initial bed levels in August 2021 are posted simultaneously, but the survey in 2021 extended much further (Fig. 5), so Fig. 11 shows the parts with the observation in 2022. As is shown in Fig. 11, Jinmeng Bay Beach is stable in terms of the morphology from August 2021 to April 2022.

The following skill model (Willmott, 1981) is used to evaluate the model performance based on validations of wave model and sediment transport model.

$$\text{skill} = 1 - \frac{\sum_{i=1}^{j} |M_{\text{s}} - D|^2}{\sum_{i=1}^{j} \left(|M_{\text{s}} - \overline{D}| + |D - \overline{D}|\right)^2}, \tag{37}$$

where M_{s} and D are the data from simulation and observation, respectively; $\overline{D}$ is the average of observed data; j is the number of observed data. A skill value as 1.0 indicates a perfect performance of the model; 0.65–1.00 for excellent models; 0.50–0.65 for very good models; 0.20–0.50 for good models; below 0.20 for poor models. Evaluation results by skill values show in Table 4.

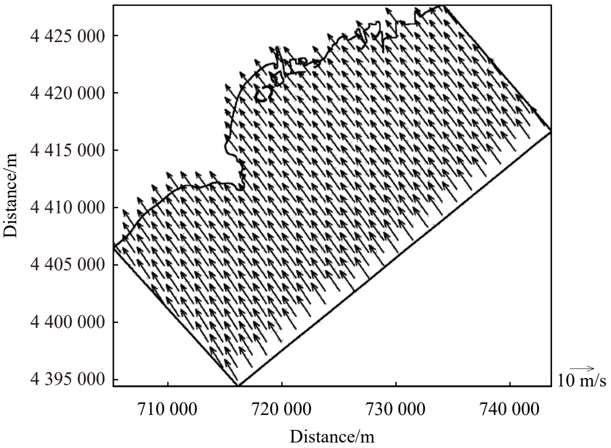

Fig. 8. Peak wind vector field during a storm on July 12, 2021.

In Table 4, both wave model and sediment transport model are of good performances in the research area. Validations for Jinmeng Bay Beach profiles turn out to be excellent, which is important for following investigations on the morphological responses of the projected beach to a flood under extreme events.

3 Results

3.1 *Flow field*

The designed flood process lasts 200 h (Fig. 7), and the peak discharge of flood occurs at 21 h. Figure 12 shows flow fields at typical moments by each scenario, including the peak flood (18 h), flood slack (21 h) and peak ebb (24 h). Figures 12a and b (excluding flood) illustrates that the hydrodynamic conditions are poor along the north-west shore of Conch Island, where the flow velocity is below 0.10 m/s generally. At the peak ebb (24 h), there is a tiny increase of the flow velocity along the target shore, because the projected beach reduces the cross-sections and accelerates the littoral currents. However, the influences on the littoral currents are limited under the weak tidal actions at the estuary.

According to Figs 12c and d (including flood), the flood dominates the hydrodynamic conditions along the north-west shore of Conch Island. The flood from EB is separated by Conch Island, where the main branch goes along the east shore of Conch Island, while the other branch turns towards Jinmeng Bay beach along the target shore. Meanwhile, the flood from WB is of a littoral trend with relatively low flow velocity. At the peak flood (18 h), the flow velocity along the east shore of Conch Island increases after the project (Fig. 12d), while the littoral branch of flood along the target shore turns weak. When the peak discharge of flood occurs, the flow velocity at the north corner of Conch Island decreases below 0.20 m/s after the project. It indicates that the projected beach restricts the flood for decreased cross-sections. At the peak ebb (24 h), the flood discharge is still large, so the flood

Table 3. Scenarios with different dynamic conditions for investigation

Scenario	Beach nourishment	Flood	Tide	Storm wind	Storm wave	Maximum sediment input/(kg·m⁻³)
1	before	excluded	included	included	included	0
2	after	excluded	included	included	included	0
3	before	included	included	included	included	0.16
4	after	included	included	included	included	0.16

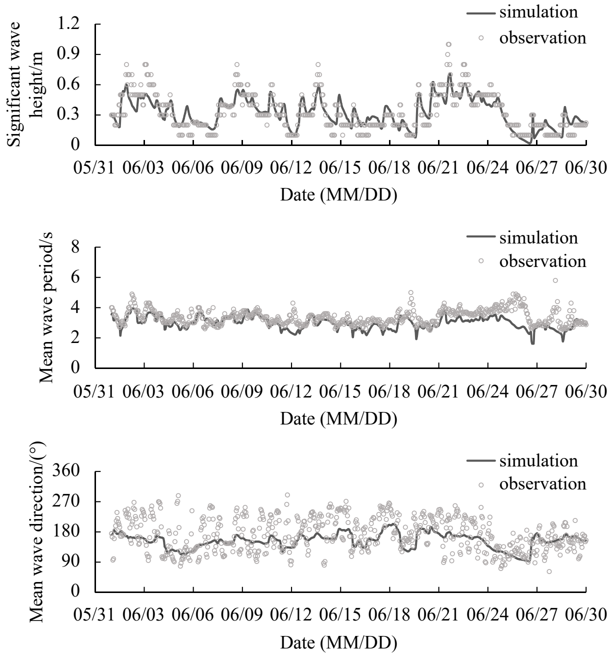

Fig. 9. Validations of significant wave height, mean wave period, and mean wave direction.

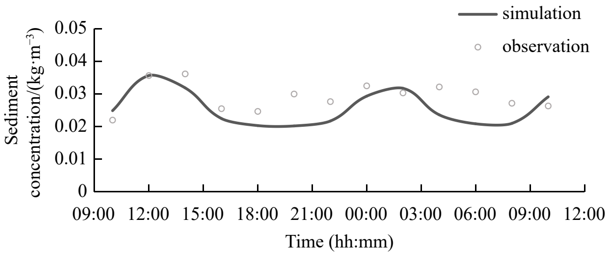

Fig. 10. Validation of sediment concentration at SS during October 18 to 19, 2016.

reverses the initial current directions along the target shore. However, the littoral branch of flood is hindered by ebb tidal currents and wave-induced currents along Jinmeng Bay Beach. Under this circumstance, the ebb tidal currents and the littoral branch of flood are confluent between Lotus Island and Conch Island, and then turn to the open sea through the channel. In a brief summary, the flood dominates the hydrodynamic conditions at the estuary under weak tidal actions, and the projected beach hinders the flood towards the open sea.

3.2 *Sediment concentration*

Figure 13 shows distributions of mean sediment concentrations during the flood process. In Scenario 1 (Fig. 13a), when flood is excluded, the mean sediment concentrations maintain the initial value about 0.02 kg/m^3 in general. According to local hydrodynamic characteristics, suspended sediments settle gradually with inadequate supplements at the estuary. Com-

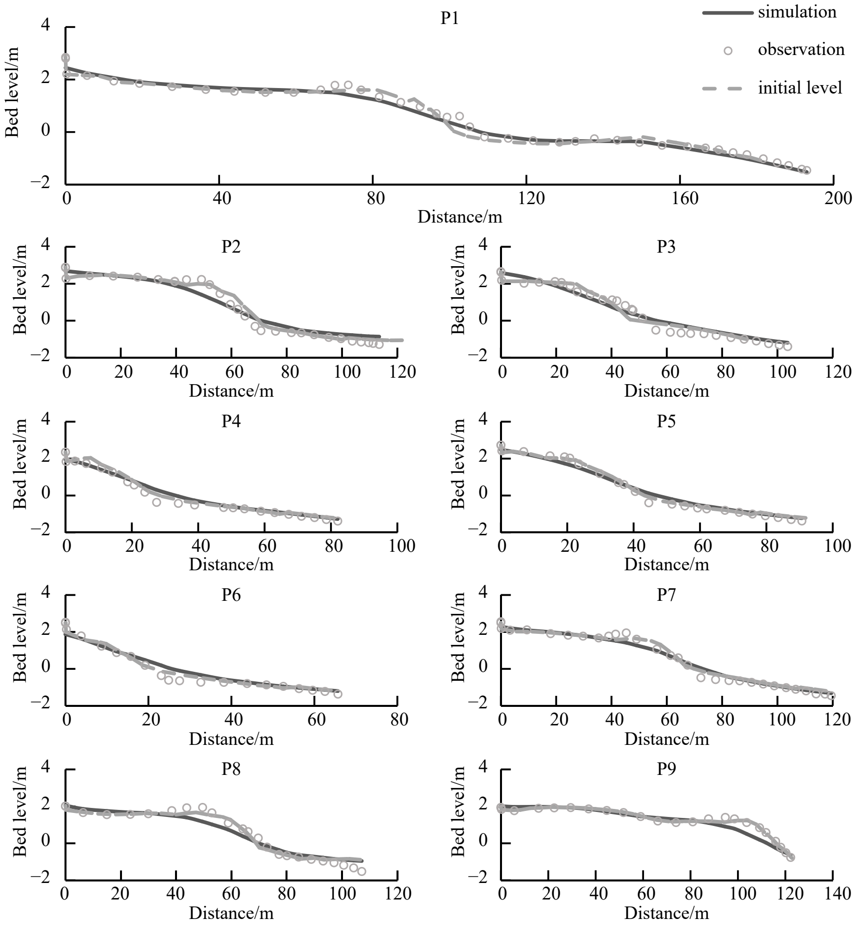

Fig. 11. Validations of beach evolution of Jinmeng Bay Beach from August 2021 to April 2022.

Table 4. Evaluation results by skill values

Model	Item	Skill value	Evaluation
Wave	significant wave height	0.90	excellent
	mean wave period	0.64	very good
	mean wave direction	0.58	very good
	sediment concentration	0.65	excellent
Sediment transport	beach profile P1	1.00	excellent
	beach profile P2	0.98	excellent
	beach profile P3	0.99	excellent
	beach profile P4	0.99	excellent
	beach profile P5	0.99	excellent
	beach profile P6	0.98	excellent
	beach profile P7	0.99	excellent
	beach profile P8	0.98	excellent
	beach profile P9	0.97	excellent

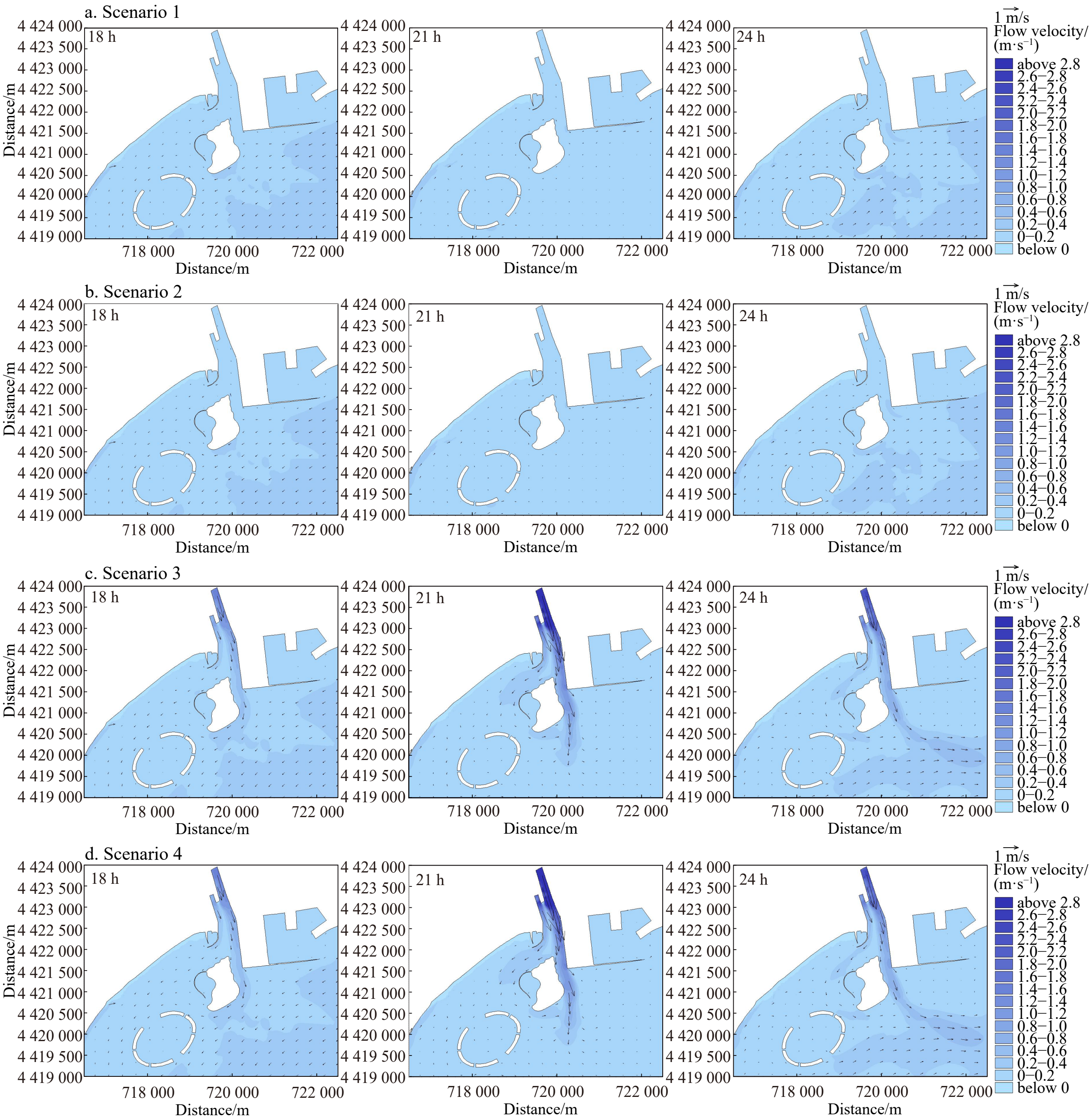

Fig. 12. Typical flow fields at 18 h, 21 h, 24 h by Scenario 1 (a), Scenario 2 (b), Scenario 3 (c), and Scenario 4 (d).

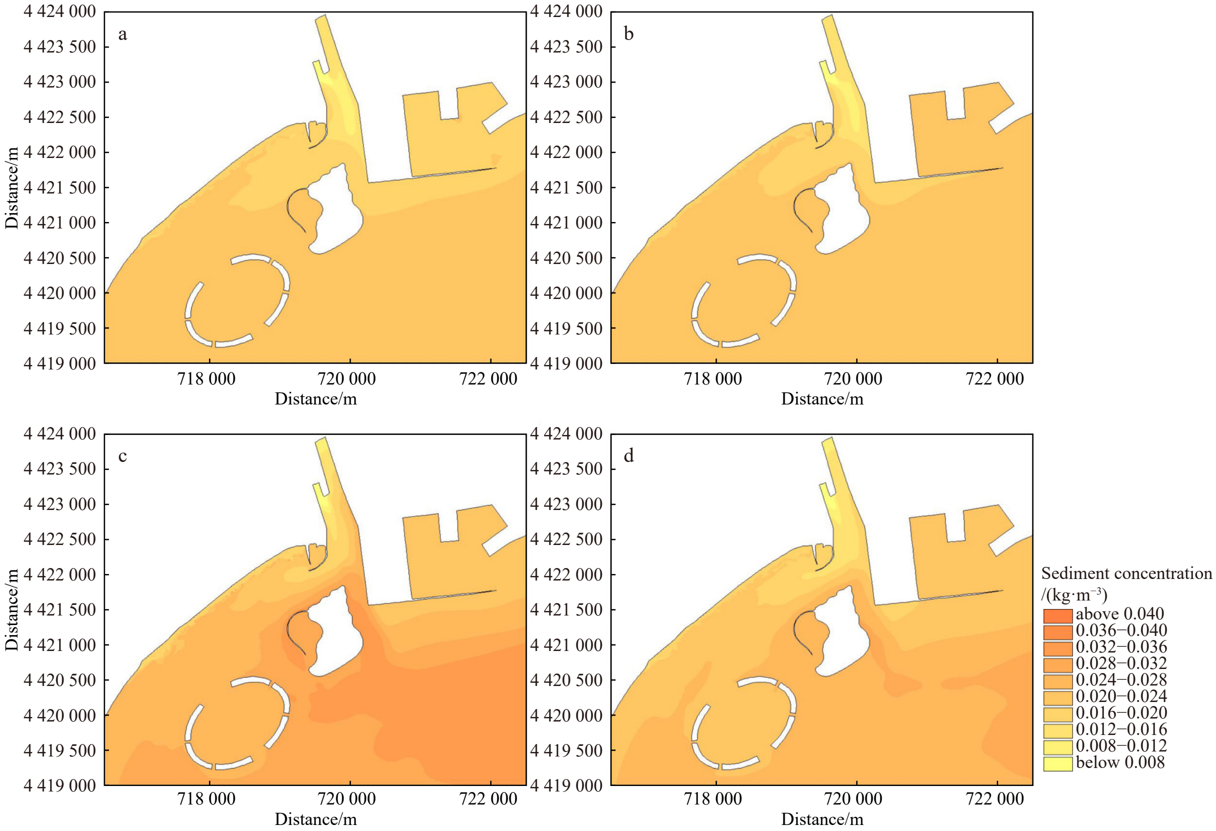

Fig. 13. Distributions of mean sediment concentrations during the flood process by Scenario 1 (a), Scenario 2 (b), Scenario 3 (c), and Scenario 4 (d).

pared with EB, WB is faced with weaker actions for its limited scales. In this situation, the sediment concentration at WB is less than 0.008 kg/m^3 particularly. After the construction of projected beach in Scenario 2 (Fig. 13b), the littoral tidal currents speed up and intensify local sediment transport along the projected beach, so the sediment concentrations are relatively higher at the estuary.

Figure 13c illustrates that the sediment input with flood generates a zone with high sediment concentration around Conch Island, and the maximum mean value is up to 0.035 kg/m^3 inside the zone. Compared with Scenario 1, it is evident that the sediment input with flood plays an important role in local sediment transport. Such an increase in sediment concentration may result from two inducements. On the one hand, the intensive flood actions contribute to massive bed scours at the estuary, and then local sediment concentration rises considerably. On the other hand, after the peak discharge of flood, tides take over the dominations of local hydrodynamic conditions gradually, and then suspended sediments accumulate at the estuary for the weak tidal actions. In Scenario 4 (Fig. 13d), there is a great decrease in sediment concentration in the research area compared with that in Scenario 3. In details, the maximum value in the high-concentration zone around Conch Island is 0.028 kg/m^3, where the decrease is up to 20%. Once the flood happens, the projected beach hinders the flood, and restricts the bed scours from the flood indirectly. Therefore, the target shore is faced with a lower risk of excessive accretion after the flood under the protection by beach nourishment.

3.3 *Morphological changes*

According to the distributions of mean sediment concentrations, the bed scours at the estuary are likely to cause additional suspended sediments, which ought to be verified by the morphological changes further. Considering that the flood process lasts 200 h, the final morphological changes at 200 h in the research area are posted in Fig. 14.

When the flood is excluded (Figs 14a and b), the erosions occur along the south and the east shores of Conch Island, where tidal currents are in relatively high velocities (Fig. 12), and the maximum erosion depth is within 0.010 00 m. The deposition just occurs at the east end of projected beach in Scenario 2 (Fig. 14b), where the maximum deposition depth is 0.000 04 m. When the flood happens (Figs 14c and d), the bed of the Tanghe Estuary suffers from flood-induced scours, and the maximum erosion depth in EB is about 0.040 00 m. The morphological changes correspond with the sediment transports in the research area, that the estuary suffers more scours in Scenario 3 than that in Scenario 4. Although the flood enhances the erosions on the south and the east of Conch Island, the sediment transport by the littoral branch of flood is hindered by the projected beach effectively. The maximum deposition depth at the east end of projected beach is about 0.000 03 m, which is close to the value in Scenario 2. Under such circumstances, the accretions result from the tidal currents rather than the flood. In fact, most suspended sediments transport to the open sea by the flood, and then the tidal currents with high sediment concentration contribute to accretions. In other words, the tidal currents can compensate a part of sediments for the loss from flood-induced scours at the estuary.

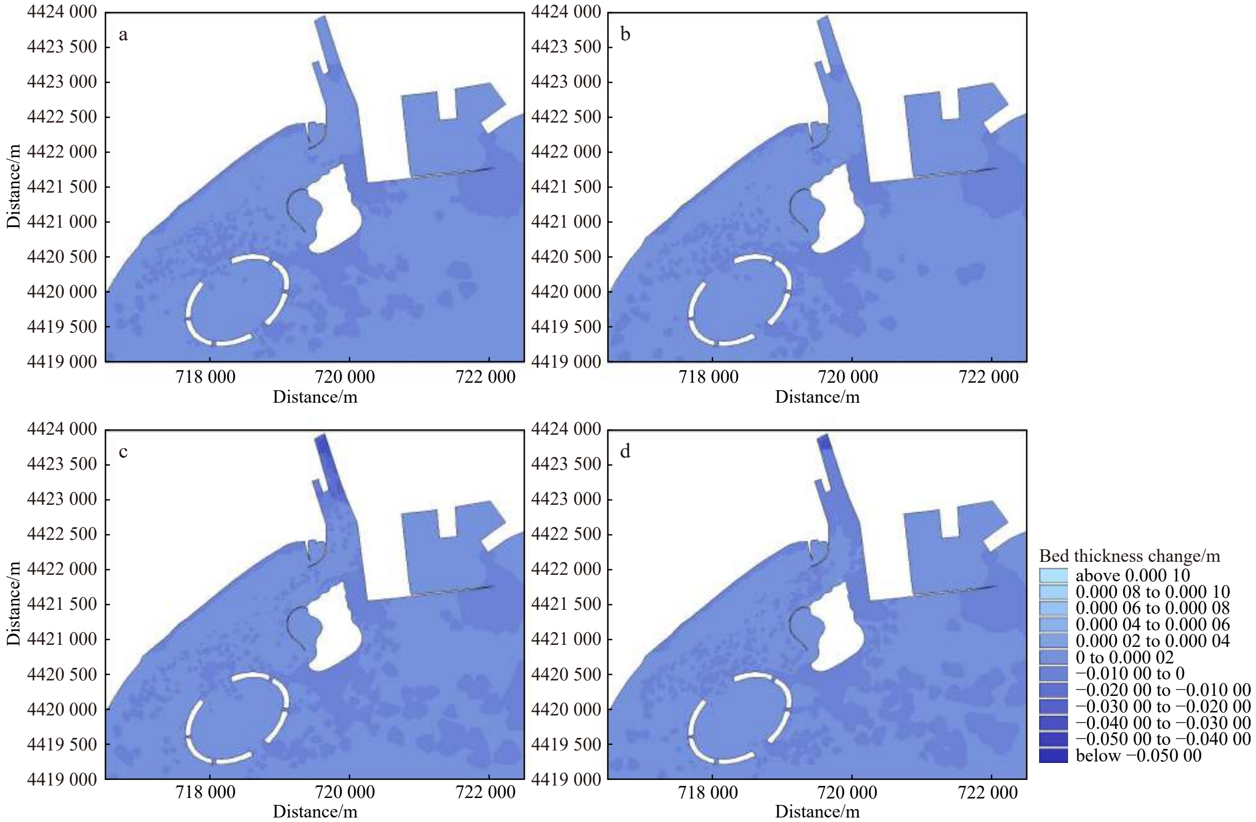

Fig. 14. Distributions of final morphological changes after the flood process by Scenario 1 (a), Scenario 2 (b), Scenario 3 (c), and Scenario 4 (d).

4 Discussion

Simulations of previous scenarios (Scenarios 1–4) are based on the real-world conditions in July 2021. To simulate extreme events, the spring tides are included. Influences on the projected beach of the components in extreme events are further discussed. In addition, considering the constructions of rubber dams at the Tanghe Estuary, the risks of local bed scours rise during the flood process, that the maximum sediment input may increase. Therefore, more values of the maximum sediment inputs are taken into accounts, including 0.50 kg/m^3, 1.00 kg/m^3, and 2.00 kg/m^3. Table 5 shows the details.

Figure 15 shows mean flow fields during the flood process for discussion. In Scenario 5 (Fig. 15a), the mean flow velocity at the estuary is in a low level (below 0.04 m/s). The variations of cross-sections at the north corner of Conch Island cause high flow velocity by about 0.18 m/s. Moreover, the sandbars along Jinmeng Bay Beach decelerate the littoral currents apparently. In Scenario 6 (Fig. 15b), the flood intensifies and dominates the hydrodynamic actions at the estuary, where the maximum mean flow velocity at the Tanghe Estuary increases to 0.25 m/s approximately. Meanwhile, the maximum mean flow velocity along the east side of Conch Island increases from 0.20 m/s to 0.23 m/s by 15%. Nevertheless, the landward storm winds have negative effects on the flood in Scenario 7 (Fig. 15c), and the maximum mean flow velocity at the Tanghe Estuary decreases to 0.23 m/s. Furthermore, the storm winds intensify the littoral currents. When the storm waves are included (Fig. 15d), wave-induced currents along Jinmeng Bay Beach are intensive, with the maximum mean flow velocity over 0.28 m/s. Meanwhile, the storm waves result in a tiny decrease on the mean flow velocities at the estuary, because the wave actions are hindered by Conch Island. The hydrodynamic characteristics along the projected beach are similar among Scenarios 6–8, which illustrates that storm winds and waves can barely affect the projected beach under the protections by Conch Island.

Figure 16 shows distributions of mean sediment concentrations during the extreme event. To show the differences between these scenarios, the representative patterns of Scenarios 6–8 are under the maximum sediment inputs as 2.00 kg/m^3. In Scenario 5, the flood is excluded, so the sediment input is 0. According to Fig. 16a, the sediment concentrations maintain as the initial value (0.02 kg/m^3) in Scenario 5. In Scenario 6 (Fig. 16b), the suspended sediments transport with flood to the open sea, and the high-concentration zone covers a considerable area. There are few cores with the maximum values as 0.28 kg/m^3 inside the zone, and the maximum value at the estuary is up to 0.20 kg/m^3.

Table 5. Scenarios with different dynamic actions for discussion

Scenario	Beach nourishment	Flood	Spring tide	Strom wind	Storm wave	Maximum sediment input concentration/(kg·m^{-3})
5	after	excluded	included	excluded	excluded	0
6	after	included	included	excluded	excluded	0.16, 0.50, 1.00, 2.00
7	after	included	included	included	excluded	0.16, 0.50, 1.00, 2.00
8	after	included	included	included	included	0.16, 0.50, 1.00, 2.00

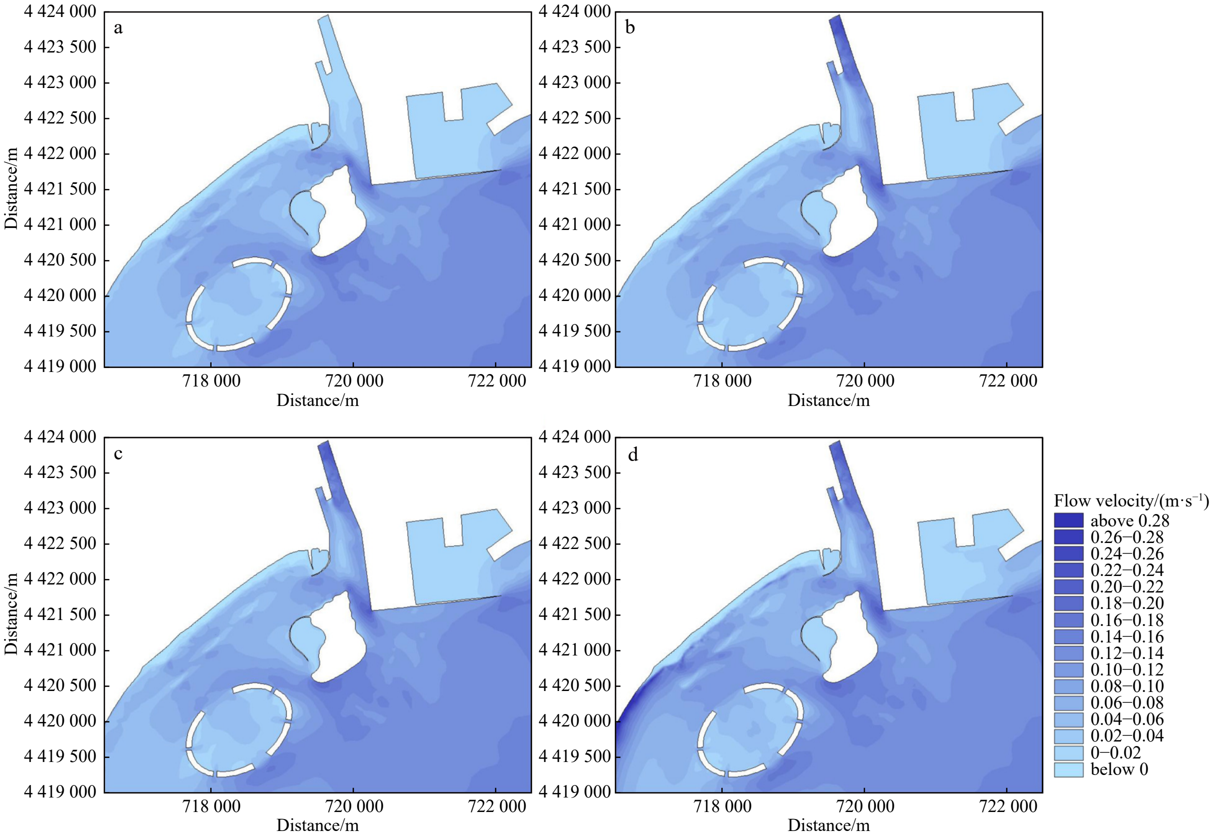

Fig. 15. Mean flow fields during the flood process by Scenario 5 (a), Scenario 6 (b), Scenario 7 (c), and Scenario 8 (d).

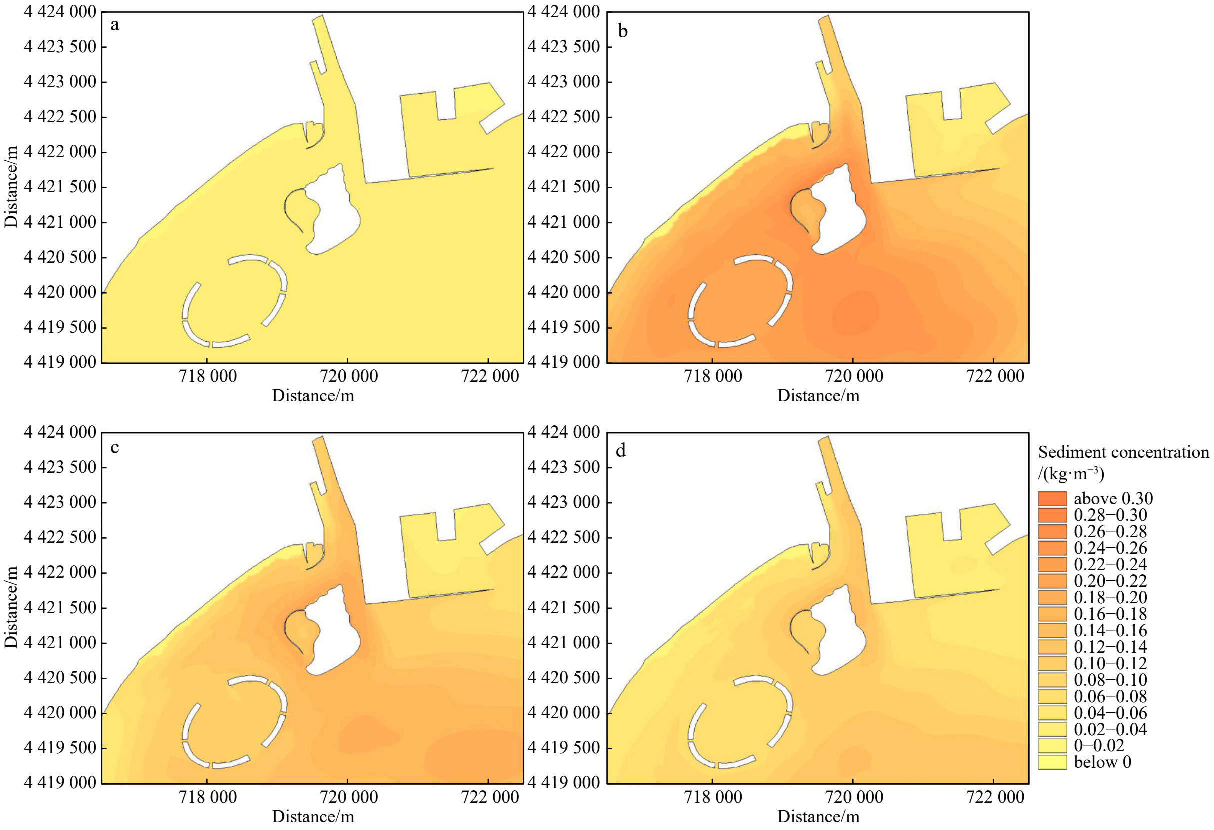

Fig. 16. Distributions of mean sediment concentrations during the flood process by Scenario 5 (a); Scenario 6 (b); Scenario 7 (c); Scenario 8 (d).

Simultaneously, the suspended sediments can barely settle under intensive tidal actions, so the spring tides may extend the high-concentration zone further. Once the storm is included, the flood actions are weakened by landward winds (Fig. 16c). The maximum sediment concentration around Conch Island declines to 0.21 kg/m^3 by 25%, and the maximum value at the estuary decreases to 0.17 kg/m^3 by 15%. When the storm waves are included (Fig. 16d), the flood can hardly reach Lotus Island due to the wave-induced littoral currents, so the high-concentration zone mainly is around Conch Island with the maximum value as 0.15 kg/m^3. Compared with Scenario 6, the maximum sediment concentration decreases by about 46% under the combined actions of storm winds and waves in Scenario 8. According to Fig. 16, the maximum mean sediment concentrations along the projected beach in Scenarios 6–8 are collected for following discussions. Table 6 shows maximum mean sediment concentrations along the projected beach in Scenarios 6–8.

As is shown in Table 6, the storm winds and waves can reduce the maximum mean sediment concentration along the projected beach by restricting flood actions. Compared with Scenario 6, the storm winds contribute to a decrease by 21% in Scenario 7, and with the combined actions of storm winds and waves, the decrease is up to 38% in Scenario 8. During the collections, the maximum mean sediment concentrations generally occur at the west end of the projected beach. Therefore, the west end of projected beach is selected as a representative position for following discussions on morphological changes.

At the end of the flood process (200 h), the deposition depths at the west end of projected beach in Scenarios 5–8 are collected. Details are as follows in Table 7. Based on the values, a relationship between the deposition depths and the maximum sediment inputs with the flood is established (Fig. 17), where Scenario 5 acts as a reference for Scenarios 6–8.

There is a quadratic polynomial relationship between the deposition depths and the maximum sediment inputs with flood in Fig. 17. The coefficient of determination, R^2, is up to 1.0 for each fitting in Scenarios 6–8. In the equations, the constant item, 0.000 000 3, represents a common condition in Scenario 5, which indicates that the position is in a deposition state even without the flood. In the extreme event, the deposition depths are related to the flood actions, because the sediment inputs with flood are main sources. Under the same sediment input, once the storm winds and waves are included, the deposition depths decrease with the weakened flood actions. With such relationships, it is accessible to estimate the deposition depths on the projected beach after the flood process in extreme events.

Table 6. Maximum mean sediment concentrations along the projected beach in Scenarios 6–8

Scenario	Maximum mean sediment concentration/(kg·m^{-3})				Average decrease compared with Scenario 6
	MSI = 0.16 kg/m^3	MSI = 0.50 kg/m^3	MSI = 1.00 kg/m^3	MSI = 2.00 kg/m^3	
6	0.032	0.078	0.146	0.281	–
7	0.028	0.062	0.111	0.210	21%
8	0.025	0.048	0.082	0.151	38%

Note: – means exclusion of the calculation; MSI is the maximum sediment input concentration.

Table 7. Deposition depths along the projected beach after the flood process

Scenario	Deposition thickness/mm				
	MSI = 0 kg/m^3	MSI = 0.16 kg/m^3	MSI = 0.50 kg/m^3	MSI = 1.00 kg/m^3	MSI = 2.00 kg/m^3
5	0. 0003	–	–	–	–
6	–	0.000 8	0.005 5	0.020 7	0.080 2
7	–	0.000 6	0.004 4	0.016 3	0.064 0
8	–	0.000 6	0.003 5	0.013 3	0.052 1

Note: – means none of the results; MSI is the maximum sediment input concentration.

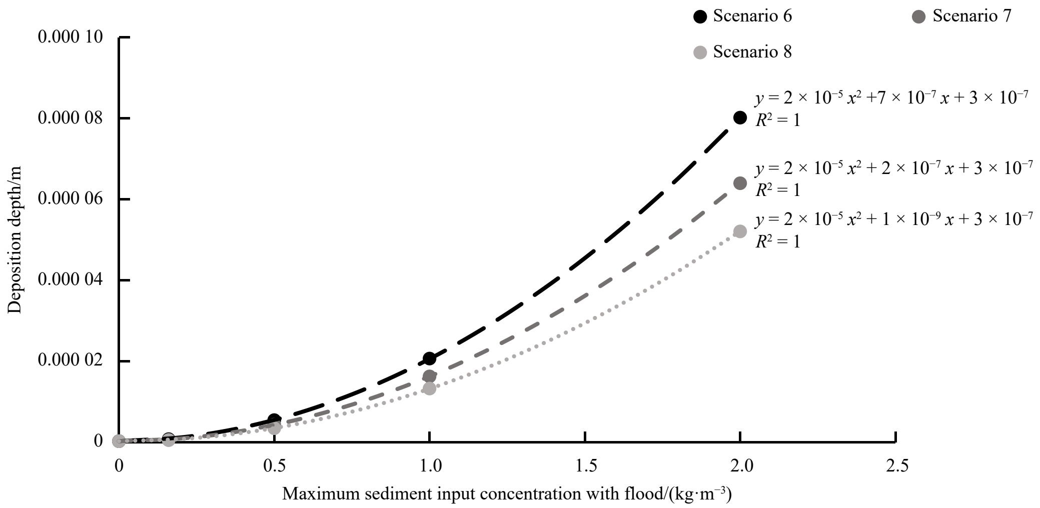

Fig. 17. Relationships between deposition depths and maximum sediment inputs with flood.

5 Conclusions

The morphological responses of the projected beach on the north-west shore of Conch Island to a flood in extreme events are investigated by field observations and numerical modelling. Based on the recent surveys on Jinmeng Bay Beach, a multi-coupled model is established, which covers the Tanghe Estuary, Conch Island, Lotus Island and Jinmeng Bay Beach. Qualitative analysis and quantitative analysis are utilized to investigations on local hydrodynamic characteristics and sediment transports. Then the impacts on the projected beach of the components in extreme events are discussed, including the flood, spring tides, storm winds, storm waves and sediment inputs. The findings are as follows.

(1) According to the field observations of Jinmeng Bay Beach, artificial islands have positive effects on coasts by hindering landward waves. Meanwhile, the structures rise the risk of excessive deposition on the projected beach.

(2) Flood dominates the hydrodynamic conditions at the estuary under weak tidal actions. Moreover, it brings massive sediment inputs and additional sediments from flood-induced scours. However, the accretions along the target shore result from the tidal currents with high sediment concentration rather than the flood.

(3) The projected beach mitigates the flood actions and restricts the flood-induced scours indirectly. Therefore, it contributes to a decrease by about 20% of the maximum mean sediment concentration during the flood process.

(4) The storm winds decelerate the flood, and decrease the maximum mean sediment concentration along the projected beach by 21%. In addition, the wave-induced currents restrict the littoral branch of flood, and the decrease of the maximum mean sediment concentration along the projected beach reaches 38% under the combined actions of storm winds and waves.

(5) A quadratic polynomial relationship between the deposition depths and the maximum sediment inputs with flood is established to estimate the morphological changes of the projected beach after the flood process in extreme events for future managements.

In this study, the designed flood process is based on the flood and the sediment concentration from records. With climate changes, the estuarine floods are of uncertainty recently. Therefore, for sustainable managements, it is essential to monitor the hydrodynamic variations in the Tanghe River, and the sediment characteristics at the estuary.

References

Ban Meina, Wu Yongxin. 2018. Flood discharging capacity of the outlet section of Nandu River based on MIKE21-FM model. South-to-North Water Transfers and Water Science & Technology (in Chinese), 16(2): 151–157

Cao Zude, Wang Yunhong. 1994. Numerical Simulation of Hydrodynamics and Sediment Transport (in Chinese). Tianjin: Tianjin University Press

Cheng Niansheng. 1997. Simplified settling velocity formula for sediment particle. Journal of Hydraulic Engineering, 123(2): 149–152, doi: 10.1061/(ASCE)0733-9429(1997)123:2(149)

Dean R G. 1991. Equilibrium beach profiles: characteristics and applications. Journal of Coastal Research, 7(1): 53–84

Han Xijun, Cao Zude, Yang Shusen. 2007. Study on scour around a structure on silt-sandy seabed by extension method of series models. Haiyang Xuebao (in Chinese), 29(1): 150–154

Han Xuejian, Kuang Cuiping, Li Yan, et al. 2022. Numerical modeling of a green tide migration process with multiple artificial structures in the western Bohai Sea, China. Applied Sciences, 12(6): 3017, doi: 10.3390/app12063017

Han Xijun, Yang Shusen, Cao Zude. 2009. Test of scouring around the man-made island under the interaction of wave and current on silty sand seabed. Port & Waterway Engineering (in Chinese), (1): 103–107

He Yanyu, Zhu Jun, Qi Hongshuai, et al. 2021. Beach restoration strategy influenced by artificial island: A case study on the west coast of Haikou. Journal of Applied Oceanography (in Chinese), 40(1): 2–11

Krone R B. 1962. Flume studies of the transport of sediment in estuarial shoaling processes. Berkeley: Hydraulic Engineering Laboratory and Sanitary Engineering Research Laboratory

Kuang Cuiping, Fan Jiadong, Dong Zhichao, et al. 2022. Influence mechanism of geomorphological evolution in a tidal lagoon with rising sea level. Journal of Marine Science and Engineering, 10(1): 108, doi: 10.3390/jmse10010108

Kuang Cuiping, Mao Xiaodan, Gu Jie, et al. 2019. Morphological processes of two artificial submerged shore-parallel sandbars for beach nourishment in a nearshore zone. Ocean & Coastal Management, 179: 104870

Kuang Cuiping, Pan Yi, Zhang Yu, et al. 2011. Performance evaluation of a beach nourishment project at west beach in Beidaihe, China. Journal of Coastal Research, 27(4): 769–783, doi: 10.2112/JCOASTRES-D-10-00184.1

Li Shan. 2015. Hainan Mannings Riyuewan Island sediment characteristics research (in Chinese)[dissertation]. Qingdao: Ocean University of China

Li Yihong. 2018. Study on the influence of three types of typical coastal structures to the adjacent beach in China (in Chinese)[dissertation]. Xiamen: The Third Institute of Oceanography, State Oceanic Administration

Li Songzhe. 2021. Study on the influence of artificial island on dynamic sediment environment and beach erosion and deposition evolution of sandy coast. The Ocean Engineering (in Chinese), 39(4): 144–153

Li Hanying, Zhang Hongyu, Wang Xia, et al. 2019. Influence on the sandy coast evolution of the ocean engineering—A case study of artificial Riyue island, Wanning city, Hainan Island. Marine Environmental Science (in Chinese), 38(4): 575–581

Lin Xueping. 2017. Influence of offshore artificial island on sandy coastal evolution (in Chinese)[dissertation]. Qingdao: The First Institute of Oceanography, State Oceanic Administration

Liu Junping, Zheng Shihan, Wu Zhengzhong, et al. 2021. Flood evolution simulation of an island area based on MIKE 11. Journal of Zhejiang University of Technology (in Chinese), 49(1): 60–65

Qinhuangdao Qinzheng Real Estate Development Co. , Ltd. 2021. The ecological renovation on the embankment of Conch Island (in Chinese)

Sheng Tianhang, Sun Dongmei, Zhang Yang. 2016. Analysis of artificial island construction influences on individual flood erosion and deposition in estuary. Journal of Waterway and Harbor (in Chinese), 37(1): 18–26

Shi Ping, Cao Linglong, Mo Wenyuan, et al. 2015. Influence of man-made island construction on the stability of the beach in the west coast of Haikou Bay. Journal of Tropical Oceanography (in Chinese), 34(5): 57–63

Smagorinsky J. 1963. General circulation experiments with the primitive equations: I. The basic experiment. Monthly Weather Review, 91(3): 99–164, doi: 10.1175/1520-0493(1963)091<0099:GCEWTP>2.3.CO;2

Song Sheng. 2014. Evolution of erosion and deposition in the eastern sea of Fenghuang Island and the application (in Chinese)[dissertation]. Qingdao: Ocean University of China

Tang Cunben. 1963. Rules of sediment movement. Journal of Hydraulic Engineering (in Chinese), (2): 1–12

Teeter A M. 1986. Vertical transport in fine-grained suspension and newly-deposited sediment. In: Mehta A J, ed. Estuarine Cohesive Sediment Dynamics. New York: Springer, 170–191

Wang Baocai. 2014. The analysis of the survey and construction of an artificial island in Qinhuangdao. Marine Information (in Chinese), 29(3): 61–64

Wang Liji, Chen Guoping, Yan Shichang. 2013a. Impact of construction of artificial island on neighboring tidal field. Port & Waterway Engineering (in Chinese), (9): 17–23

Wang Yaping, Voulgaris G, Li Yan, et al. 2013b. Sediment resuspension, flocculation, and settling in a macrotidal estuary. Journal of Geophysical Research: Oceans, 118(10): 5591–5608, doi: 10.1002/jgrc.20340

Willmott C J. 1981. On the validation of models. Physical Geography, 2(2): 184–194, doi: 10.1080/02723646.1981.10642213

Wu Jin. 1980. Wind-stress coefficients over sea surface near neutral conditions—A revisit. Journal of Physical Oceanography, 10(5): 727–740, doi: 10.1175/1520-0485(1980)010<0727:WSCOSS>2.0.CO;2

Wu Jin. 1994. The sea surface is aerodynamically rough even under light winds. Boundary-Layer Meteorology, 69(1): 149–158

Xiao Zheyu. 2021. Research on sediment recycling nourishment technology and coastal evolution under the influence of artificial island (in Chinese)[dissertation]. Xiamen: The Third Institute of Oceanography, State Oceanic Administration

Xiao Zheyu, Qi Hongshuai, Cai Feng, et al. 2022. The impact of artificial island construction on sedimentary characteristics and sediment transport in the Haikou Bay. Haiyang Xuebao (in Chinese), 44(3): 137–146

Xie Yaqiong, Liu Songtao, Liu Jimin, et al. 2013. Ecological restoration design of Jinmeng Bay Beach in Qinhuangdao. Marine Geology Frontiers (in Chinese), 29(2): 79–86

Zhang Yang. 2013. Numerical simulation research on the impacts of man-made island on flood propagation and erosion-deposition of estuary (in Chinese)[dissertation]. Tianjin: Tianjin University

Zhang Yu, He Lulu, Kuang Cuiping, et al. 2012. Numerical study of shoreline changes by emergency beach nourishment project at the Middle Beach of Beidaihe, China. Acta Oceanologica Sinica, 31(1): 125–133, doi: 10.1007/s13131-012-0184-1

Zhang Daheng, Shi Lianqiang, Gong Zhaohui, et al. 2022. Evolution characteristics of beach erosion and accretion at the Riyue Bay under the combined impacts of winter waves and artificial island. Journal of Tropical Oceanography (in Chinese), 41(4): 71–81

Zhong Xiaojing. 2017. Morphodynamics of the beaches around Hainan Island: the normal process, the influences of extreme events and artificial island construction (in Chinese)[dissertation]. Shanghai: East China Normal University

Zhong Chao, Shi Hongyuan, Sui Yi, et al. 2021. The causes and protective measures of coastal erosion in China. Ocean Development and Management (in Chinese), 38(6): 42–45

Zou Kai. 2020. Research on the man-made island's influence on beach erosion under typhoon: based on the case of Haikou Bay under typhoon Kalmaegi (in Chinese)[dissertation]. Guangzhou: South China University of Technology